A low-Mach volume-of-fluid model for the evaporation of suspended droplets in buoyancy-driven flows

Edoardo Cipriano [a],*, Alessio Frassoldati [a], Tiziano Faravelli [a], Stéphane Popinet [b], Alberto Cuoci [a]

[a] *CRECK Modeling Lab, Department of Chemistry, Materials, and Chemical Engineering "G. Natta", Politecnico di Milano, Piazza Leonardo da Vinci, 32, Milano, 20133, Italy*

[b] *Institut Jean Le Rond d'Alembert, CNRS UMR 7190, Sorbonne Université, Paris, 75005, France*

ARTICLE INFO

ABSTRACT

This study introduces a comprehensive numerical model capable of simulating the evaporation of suspended droplets under different gravity conditions. Unlike previous studies, this work provides a detailed description of the multicomponent evaporation process by integrating: (i) interface-resolved evaporation; (ii) suspension by the action of the surface tension force, and (iii) variable physical properties. The model effectively captures complex phenomena such as thermal expansion, natural convective fluxes, and liquid internal recirculation, which cannot be directly resolved using more widespread spherically-symmetric models. Validation against experimental data confirms the model's accuracy in predicting the droplet evaporation dynamics, and its utility in resolving discrepancies between prior numerical simulations results and experimental data. The model was implemented in the Basilisk framework; both the code and the simulations setups are freely available on the Basilisk sandbox.

1. Introduction

The evaporation of liquid droplets is ubiquitous in nature and in engineering applications. Understanding the dynamics of evaporating droplets has a direct impact on diverse fields, ranging from the analysis of wave breaking [1] to the combustion of liquid fuels [2]. Accurately designing burners and other industrial equipment necessitates knowledge of the liquid droplets' lifetime, which varies with the initial diameter, composition, and operating conditions.

The fundamental importance of the problem pushed the experimental investigation of droplet evaporation in different conditions. Nomura et al. [3] studied n-heptane in microgravity at elevated pressure and temperature. Verwey and Birouk [4] and Murakami et al. [5] studied the evaporation of n-decane droplets suspended on a solid fiber in normal gravity, focusing on the effect of the initial droplet diameter on the consumption rate. Ghassemi et al. [6] analyzed pure and binary droplets of n-heptane and n-hexadecane at different ambient temperatures and pressures, while Daïf et al. [7] focused on n-heptane/n-decane droplets in forced convection.

Despite the abundance of papers on the combustion of liquid droplets [8–11], literature on droplet evaporation remains scarce. This may be due to the inherent complexity of carrying out such experiments isolating the effect of droplet evaporation from additional physical phenomena. The typical experimental configuration consists of a droplet, suspended by a solid fiber, inside a furnace that is maintained at constant temperature. In these conditions, the evaporation process can be strongly influenced by the radiation from the furnace walls, the heat conduction through the solid fiber, and the residual gravity (if the experiment aims to be in microgravity conditions). These limitations call for detailed mathematical models, which describe the evaporation of droplets at different operative conditions, in order to deepen our understanding of the process by isolating and studying each physical phenomenon separately. These models also serve as a tool to drive the experimental investigation and to explain discrepancies between the literature data and simplified models.

Most of the current models for droplet evaporation rely on the spherical symmetry assumption: the droplet is assumed to be perfectly spherical and the complex set of multidimensional equations reduces to a 1D model [2,12,13]. This class of models is convenient for the limited computational time requested, but it is unable to directly resolve multidimensional phenomena, such as droplet deformation, buoyancy-driven flows, and liquid internal recirculation. Furthermore, they can be used only for simulations of single isolated droplets, and they are unable to resolve the interactions between multiple droplets.

Due to these limitations, several models for the simulation of phase change using multiphase CFD have been proposed during the last 20 years. These models are based on different descriptions of the

---

* Corresponding author.
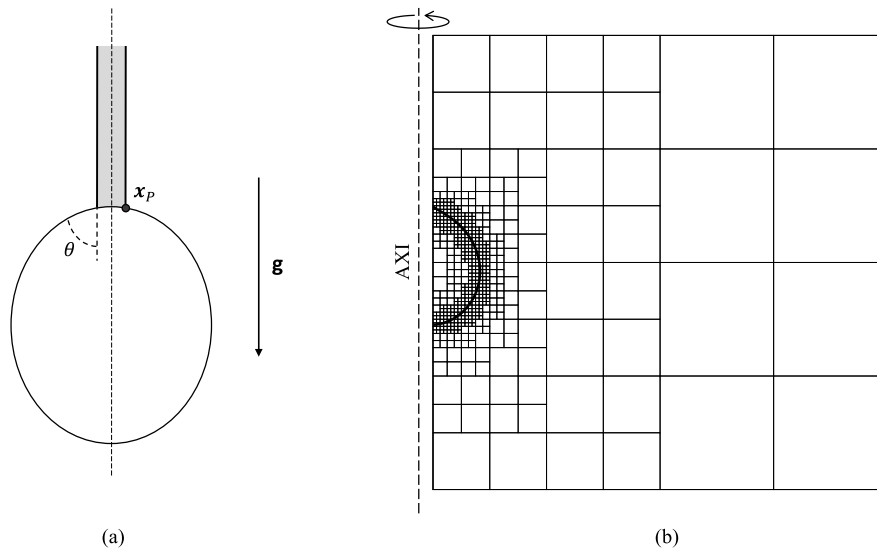*E-mail address:* edoardo.cipriano@polimi.it (E. Cipriano).

Fig. 1. Simulation setup for suspended droplets in normal gravity conditions. Schematic representation of the droplet suspended on a solid fiber, with contact angle θ, pinning point $\mathbf{x}_p$, and gravity $\mathbf{g}$ (a); simulation setup for the axial-symmetric suspended droplet configuration, using an adaptive grid (b).

multiphase systems, such as the front tracking model [14], the level set approach [15], and the volume-of-fluid [16–18]. Most of these models are based on the assumption of constant physical properties, which limits their applicability to benchmark phase change simulations, used for the validation of the model itself. While these simulations are essential to test the numerical methods, descriptions of realistic droplets require extending these models including variable physical properties and relaxing the hypothesis of incompressible flow. Especially in low-Mach multicomponent systems, the thermodynamic and transport properties are strongly affected by variations in temperature and composition. To the author's knowledge, the first attempt to combine a multiphase phase change model with a variable-properties formulation was made by Wang et al. [19], focusing on pure droplets in convective conditions. Scapin et al. [20] used a variable properties formulation to study the evaporation of droplets in turbulent conditions. More recently, Mialhe et al. [21] proposed a variable-properties evaporation model, based on the level set approach, which focuses on a variable surface tension formulation for the simulation of Marangoni convection. During the last year, the extension of interface-resolved phase change models to all-Mach formulations has been proposed by Wenzel and Arienti [22] and Bibal et al. [23].

In this work, we extend a VOF-based multicomponent phase change model [24], including variable thermodynamic and transport properties, low-Mach compressibility effects, and droplet suspension by the action of the surface tension force. We propose the first detailed multidimensional model for the simulation of realistic droplets both in microgravity and suspended at different gravity conditions, resolving thermal expansion effects, buoyancy-driven flows, and liquid internal recirculation. The mathematical model and its numerical discretization is presented in Section 2, while the results obtained from the numerical simulations are reported in Section 3.

2. Numerical model

The numerical model presented in this work is the extension of an incompressible Volume-Of-Fluid (VOF) based phase change model for multicomponent evaporation [24]. The previous model assumes constant properties, and focuses on the numerical methods for solving the transport equations that describe the system, including a proper way to enforce the gas–liquid interface boundary conditions. Here we expand that model to include variable thermodynamic and transport properties, low-Mach compressibility effects, interface radiation, and

a strategy for achieving stable suspension of the droplet on a solid fiber, mimicking the experimental configuration sketched in Fig. 1. The solid fiber is considered just from the geometrical point of view, meaning that the heat transfer between the solid and the gas–liquid system is neglected. This approximation is valid for sufficiently thin solid fibers. Although this work focuses on the evaporation of isolated droplets, the model formulation is general and it can be used for generic phase change in a two-phase system. The following sections introduce the assumptions and the governing equations of the model, with the corresponding interface boundary conditions (Sections 2.1 and 2.2); Sections 2.3 and 2.4 describe the details of the variable properties formulation and the droplet suspension strategy, while the numerical solution is summarized in Section 2.5.

2.1. Mathematical formulation

The control volume over which the system of equations is solved comprises two immiscible phases separated by a zero-thickness interface. The characteristic function H is introduced to distinguish between the two phases:

$$H(\mathbf{x}, t) = \begin{cases} 1 & \text{if liquid phase} \\ 0 & \text{if gas phase} \end{cases} \tag{1}$$

where $\mathbf{x}$ and t indicate the space and time coordinates, respectively. Drew [25] demonstrated that the transport of the characteristic function by the interface velocity $\mathbf{u}_\Gamma$ obeys the condition:

$$\frac{DH}{Dt} = \frac{\partial H}{\partial t} + \mathbf{u}_\Gamma \cdot \nabla H = 0 \tag{2}$$

The governing equations for each phase derive from a set of conservation laws on mass, momentum, chemical species, and enthalpy, which can be written for each phase k in the general form [26,27]:

$$\frac{\partial \rho_k}{\partial t} + \nabla \cdot \left(\rho_k \mathbf{u}_k \right) = 0 \tag{3}$$

$$\frac{\partial \rho_k \mathbf{u}_k}{\partial t} + \nabla \cdot \left(\rho_k \mathbf{u}_k \otimes \mathbf{u}_k \right) = -\nabla \cdot \boldsymbol{\tau}_k - \nabla p_{d,k} - \mathbf{g} \cdot \mathbf{x} \nabla \rho_k \tag{4}$$

$$\frac{\partial \rho_k \omega_{i,k}}{\partial t} + \nabla \cdot \left(\rho_k \omega_{i,k} \mathbf{u}_k \right) = -\nabla \cdot \mathbf{j}_{i,k} \tag{5}$$

$$\frac{\partial \rho_k h_k}{\partial t} + \nabla \cdot \left(\rho_k h_k \mathbf{u}_k \right) = \nabla \cdot \left(\lambda_k \nabla T_k \right) - \nabla \cdot \left(\sum_{i=1}^{NS} h_{i,k} \mathbf{j}_{i,k} \right) + \frac{Dp_k}{Dt} - \boldsymbol{\tau}_k : \nabla \mathbf{u}_k \tag{6}$$

where ρ is the density field, $\mathbf{u}$ is the velocity field, $p_d = p - \rho \mathbf{g} \cdot \mathbf{x}$ is the pressure without the hydrostatic contribution, $\mathbf{g}$ is the gravitational

acceleration, ω_i is the mass fraction of each chemical species i, and h is the sensible enthalpy. The viscous stress tensor is computed neglecting the compressible part: $\tau = -\mu(\nabla\mathbf{u} + (\nabla\mathbf{u})^T)$, where μ is the dynamic viscosity. The heat conduction term is calculated using Fourier's law, while the species diffusive flux $\mathbf{j}_i$ is obtained from a modified Fick's law, as explained in Section 2.3.

Eqs. (3)–(6) are derived for a control volume which comprises only the pure phase k, resulting in equations per unit of volume of the k–th phase. These equations must be combined with appropriate gas–liquid interface boundary conditions. Integrating Eqs. (3)–(6) over the interface we obtain a set of equations which are used to characterize the interface temperature, mass fractions, mole fractions, and the vaporization rate per unit of surface $\dot{m}_i$ for each chemical species. Introducing the jump notation for a generic quantity ϕ: $[\phi]_\Gamma = \phi_l - \phi_g$, the set of gas–liquid interface jump conditions for velocity, pressure, mass, species, and enthalpy, is obtained [28,29]:

$$[\mathbf{u}]_\Gamma \cdot \mathbf{n}_\Gamma = \dot{m}\,[1/\rho]_\Gamma \tag{7}$$

$$[p]_\Gamma = \sigma\kappa - \dot{m}[\mathbf{u}]_\Gamma \cdot \mathbf{n}_\Gamma + [\tau \cdot \mathbf{n}_\Gamma] \cdot \mathbf{n}_\Gamma \tag{8}$$

$$\dot{m}[\mathbf{u}]_\Gamma \cdot \mathbf{t}_\Gamma + [\tau \cdot \mathbf{n}_\Gamma] \cdot \mathbf{t}_\Gamma = \mathbf{t}_\Gamma \cdot \nabla_\Gamma \sigma \tag{9}$$

$$[\rho(\mathbf{u} - \mathbf{u}_\Gamma) \cdot \mathbf{n}_\Gamma]_\Gamma = 0 \tag{10}$$

$$[\rho\omega_i(\mathbf{u} - \mathbf{u}_\Gamma) \cdot \mathbf{n}_\Gamma + \mathbf{j}_i \cdot \mathbf{n}_\Gamma]_\Gamma = 0 \tag{11}$$

$$[\lambda\nabla T \cdot \mathbf{n}_\Gamma]_\Gamma = \sum_{i=1}^{NLS} \dot{m}_i[h_i]_\Gamma + \dot{q}_{rad} \tag{12}$$

where $\mathbf{n}_\Gamma$ is the interface normal, pointing outward from the liquid phase, while $\mathbf{t}_\Gamma$ is the interface tangent vector. The velocity jump (Eq. (7)) derives from the strong expansion due to the phase change, which leads to the Stefan flow. The pressure jump in Eq. (8) contains the recoil pressure term [21] and the surface tension contribution, where κ is the interface curvature while σ is the surface tension coefficient. The tangential momentum jump (Eq. (9)) contains the Marangoni effect, which is characterized by the operator ∇_Γ, indicating the gradient along the tangential direction of the interface [21]. Eqs. (10) and (11) are Rankine–Hugoniot relations which express the total mass conservation, and the mass conservation for each chemical species, across the interface. Eq. (12) states that the thermal conduction at the interface is balanced by heat removed by the evaporation (with NLS the total number of liquid species) and by the radiation flux at the interface $\dot{q}_{rad}$. The radiation is computed as in Thijs et al. [30]: $\dot{q}_{rad} = \epsilon\sigma_{SB}(T_{bulk}^4 - \hat{T}^4)$, where σ_{SB} is the Stefan–Boltzmann constant, ϵ is the emissivity of the liquid fuel, while T_{bulk} is the gas phase bulk temperature. This set of jump conditions is closed by including the thermodynamic equilibrium:

$$[f_i]_\Gamma = 0 \tag{13}$$

$$[T]_\Gamma = 0 \tag{14}$$

which indicate the equality of the fugacity f_i of each chemical species in the two phases, and the continuity of the temperature across the interface [31].

2.2. Assumptions and final form of the governing equations

Different approaches can be used to enforce the jump conditions (Eqs. (7)–(14)) in the governing equations (Eqs. (3)–(6)). The choice mainly depends on the numerical method used for the solution of the two-phase system. The level set method employs a *jump condition formulation*, using the Ghost Fluid Method [32] to impose the jump conditions directly in the values of the fields being solved. The volume-of-fluid method, instead, introduces the jump conditions directly into the governing equations in the form of source terms, according to the

whole domain formulation. The interested reader can refer to [33], and to [34, pag. 37] for a detailed discussion about the different methods.

Using the whole domain formulation, we rewrite Eqs. (3), (5) and (6), multiplying each equation by the respective characteristic function H_k, where $H_l = H$ and $H_g = 1 - H$, and introducing the relationship between the interface surface density δ_Γ and the characteristic function: $\nabla H = -\mathbf{n}_\Gamma \delta_\Gamma$. Following the procedure used by Yeoh and Tu [35] and exploiting Eqs. (10) and (11) we obtain the two-field form of the governing equations:

$$\frac{\partial H}{\partial t} + \mathbf{u}_l \cdot \nabla H = -\frac{\dot{m}}{\rho_l} \tag{15}$$

$$\frac{\partial H_k\rho_k}{\partial t} + \nabla \cdot (H_k\rho_k\mathbf{u}_k) = -\dot{m}_k\delta_\Gamma \tag{16}$$

$$H_k\rho_k\frac{D\omega_{i,k}}{Dt} = -\nabla \cdot (H_k\mathbf{j}_{i,k}) + \dot{m}_k\omega_{i,k}\delta_\Gamma - \dot{m}_{i,k}\delta_\Gamma \tag{17}$$

where the total vaporization rate per unit of surface $\dot{m}$ is the sum of the vaporization rates for each chemical species $\dot{m}_i$. Note that the signs of the source terms depend on the side of the interface as: $\dot{m} = \dot{m}_l = -\dot{m}_g$. Similarly, we re-write the enthalpy Eq. (6) assuming Newtonian fluids, negligible viscous effects and pressure work term, and low-Mach number. According to these assumptions, the enthalpy equation is written for the temperature field as:

$$H_k\rho_k Cp_k\frac{DT_k}{Dt} = \nabla \cdot (H_k\lambda_k\nabla T_k) - H_k\left(\sum_{i=1}^{NS} Cp_{i,k}\mathbf{j}_{i,k}\right) \cdot \nabla T_k + \dot{q}_{\Gamma,k}\delta_\Gamma \tag{18}$$

where Cp is the mixture heat capacity, Cp_i is the heat capacity of a single species, λ is the thermal conductivity, and $\dot{q}_\Gamma$ is the interface heat conduction term, which is calculated for each phase from the interface gradient as: $\dot{q}_{\Gamma,k} = \lambda_k\nabla T_k \cdot \mathbf{n}_\Gamma$. The sign depends on the side of the interface also in this case.

Conversely from the scalar transport equations, the Navier–Stokes equations are solved using a one-field formulation. Using this approach, a single set equation is written for the whole control volume, with properties and variables weighted on the characteristic function [36]. Neglecting the Marangoni convection from the jump condition (Eq. (9)) the one-field Navier–Stokes equations are written as follows.

$$\nabla \cdot \mathbf{u} = -\frac{1}{\rho}\frac{D\rho}{Dt} \tag{19}$$

$$\rho\frac{D\mathbf{u}}{Dt} = -\nabla \cdot \tau - \nabla p_d - \mathbf{g} \cdot \mathbf{x}\nabla\rho + \left(\sigma\kappa - \dot{m}^2[1/\rho]_\Gamma\right)\mathbf{n}_\Gamma\delta_\Gamma \tag{20}$$

The velocity jump (Eq. (7)) is not included in the continuity equation because it is directly imposed in the velocity field. This strategy improves the numerical solution of the system (see Section 2.5 for details). The variables appearing in the source terms of the governing Eqs. (15)–(20) are obtained by coupling the jump conditions in a non-linear system of equations [24]:

$$\begin{cases} \dot{m}_i = \dot{m}\hat{\omega}_{i,l} + \mathbf{j}_{i,l} \cdot \mathbf{n}_\Gamma = \dot{m}\hat{\omega}_{i,g} + \mathbf{j}_{i,g} \cdot \mathbf{n}_\Gamma \\ \sum_{i=1}^{NLS} \dot{m}_i\Delta h_{ev,i} + \dot{q}_{rad} = \lambda_l\nabla T_g \cdot \mathbf{n}_\Gamma - \lambda_g\nabla T_l \cdot \mathbf{n}_\Gamma \\ P\hat{x}_{i,g} = P_{vap,i}(\hat{T})\hat{x}_{i,l} \end{cases} \tag{21}$$

where $\hat{\omega}_i$ and $\hat{x}_i$ are the interface mass fractions and mole fractions, respectively, while $\hat{T}$ is the interface temperature. The chemical equilibrium conditions, *i.e.* equality of fugacity, is here simplified by assuming an ideal gas phase, an ideal liquid mixture, negligible Poynting correction, and using Antoine's law to calculate the vapor pressure $P_{vap,i}$ of each chemical species.

2.3. Challenges of the variable properties formulation

Extending the framework proposed by Cipriano et al. [24] with variable properties involves the introduction of: (i) equations and correlations which allow the thermodynamic and transport properties to be computed; (ii) additional relevant terms in the governing equations; (iii) corrections for the diffusive fluxes in order to enforce mass conservation. The properties of interest were introduced in the previous

sections. Given a generic property, we can distinguish the one-field property ϕ from the phase property ϕ_k. The one-field properties are used for the solution of the Navier–Stokes equations, and they are computed by a simple arithmetic average, based on the characteristic function:

$$\phi = H\phi_l + (1 - H)\phi_g \tag{22}$$

while the phase properties must be computed as a function of the thermodynamic state of the mixture:

$$\phi_k = f(P, T_k, x_{i,k}) \tag{23}$$

where P is the thermodynamic pressure of the system, which can be assumed to be constant for low-Mach flows, T_k is the temperature of the phase k, while $x_{i,k}$ are the mole fractions of the same phase. Each phase property is computed using the OpenSMOKE++ library [37], which calculates the gas phase properties using data from the CHEMKIN database [38], or following the procedures proposed by Wang and Frenklach [39]. Unavailable thermodynamic data are estimated by group additivity methods [40]. The liquid properties are obtained from correlations reported in engineering handbooks such as Reid et al. [31]. This approach for the calculation of the variable properties was previously adopted and validated by Cuoci et al. [41] for the simulation of laminar flames and by Cuoci et al. [12] for spherically-symmetric droplet combustion, including the liquid phase. The only properties which are kept constant in space and time during the simulations are the emissivity ϵ, used for the interface radiation, and the surface tension coefficient σ, which is considered to be constant because Marangoni convection is neglected. The small variations in the shape of the droplet due to a time-variable surface tension coefficient do not affect the results of this paper appreciably.

Among the physical properties that we compute as in Eq. (23), density and diffusivity require special care to avoid mass conservation issues. In particular, the density changes must be counteracted by volume changes to enforce mass conservation. This problem reduces to using a proper strategy to compute the density Lagrangian derivative in Eq. (19). In this work we use the same approach proposed by Pember et al. [42] for single phase low-Mach reactive flows, which assumes that the pressure gradients are negligible with respect to the temperature and mass fraction gradients, filtering out acoustic waves which are assumed to travel at infinite speed [43]. This is a common approximation for low-Mach systems, and it allows to significantly simplify the system of equations removing the two-way coupling between continuity and energy equations discussed by Saade et al. [44]. Therefore, the density Lagrangian derivative for each phase is computed as:

$$\nabla \cdot \mathbf{u}_k = -\frac{1}{\rho}\frac{D\rho}{Dt}\bigg|_k = \beta_k \frac{DT_k}{Dt} + M_{w,k}\sum_{i=1}^{NS}\frac{1}{M_{w,i}}\frac{D\omega_{i,k}}{Dt} \tag{24}$$

This equation is used in the one-field continuity Eq. (19) averaging the contribution of the gas and the liquid phases using the same arithmetic average used for any other one-field property (22). The term β in Eq. (24) is the thermal expansion coefficient, which is obtained from the ideal gas approximation in the gas phase, and computed directly from its definition in the liquid phase:

$$\beta_g = \frac{1}{T_g} \qquad \beta_l = -\frac{1}{\rho_l}\frac{d\rho_l}{dT} \tag{25}$$

while M_w and $M_{w,i}$ are the mixture molecular weight and the molecular weight of the single chemical species, respectively. Eq. (24) is used both for the gas and for the liquid phase. However, in liquid phase we assume that the density changes due to the temperature gradients dominate over composition effects [19]. Therefore, the last term on the RHS, which is derived in Eq. (24) under the hypothesis of ideal gas, vanishes in liquid phase. This is always true for pure liquid droplets, while it is generally valid for multicomponent droplets as well.

The diffusive fluxes $\mathbf{j}_{i,k}$ in Eq. (11), (17) and (21) are computed using Fick's law, which is exact only for binary mixtures (and for

multicomponent systems with equal diffusivities). When Fick's law is applied to multicomponent mixtures, it must be corrected in order to ensure that the sum of the diffusive fluxes of all the species is null. The diffusivity of each species is computed from the binary diffusion coefficient in each phase $\mathcal{D}_{ij,k}$ using the Hirschfelder and Curtiss approximation [45]:

$$\mathcal{D}_{i,k} = \frac{\sum_{j\neq i} x_{j,k} M_{w,j}}{M_{w,k}\sum_{j\neq i}\frac{x_{i,k}}{\mathcal{D}_{ij,k}}} \tag{26}$$

which results in diffusivities which are different for every chemical species, and molar based. According to this definition, the final form of the diffusive flux $\mathbf{j}_{i,k}$ is:

$$\mathbf{j}_{i,k} = \mathbf{j}_{i,k}^F - \omega_{i,k}\mathbf{j}_{i,k}^C = -\rho_k \mathcal{D}_{i,k}\frac{M_{w,i}}{M_{w,k}}\nabla x_{i,k} + \omega_{i,k}\sum_{i=1}^{NS}\rho_k \mathcal{D}_{i,k}\frac{M_{w,i}}{M_{w,k}}\nabla x_{i,k} \tag{27}$$

where $\mathbf{j}_{i,k}^F$ is the molar based diffusive flux computed using the Fick's law, while $\mathbf{j}_{i,k}^C$ is the diffusion correction term, which is redistributed based on the mass fraction of each chemical species, following the same approach proposed by Coffee and Heimerl [46]. By doing so, the sum of the diffusive fluxes $\mathbf{j}_{i,k}$ is equal to zero. This form of the diffusive flux can be directly used in Eqs. (18) and (21). Conversely, since Eq. (17) is solved for the mass fractions, the diffusive flux in Eq. (27) is re-written in terms of mass fractions [see 26, pag. 534 for the conversions] in order to preserve the implicit part of the transport equation:

$$H_k\rho_k\frac{D\omega_{i,k}}{Dt} = \nabla\cdot(H_k\rho_k\mathcal{D}_{i,k}\nabla\omega_{i,k}) + \nabla\cdot\left[H_k\left(\mathbf{j}_{i,k}^M + \mathbf{j}_{i,k}^C\right)\omega_{i,k}\right] + \dot{m}\omega_i\delta_\Gamma - \dot{m}_i\delta_\Gamma \tag{28}$$

The additional term on the RHS is equivalent to an additional convective flux, it includes the total diffusive fluxes contribution $\mathbf{j}_{i,k}^C$, and the correction that arises due to the conversion from mole fraction gradients to mass fraction gradients: $\mathbf{j}_{i,j}^M = \rho_k\mathcal{D}_{i,k}\nabla M_{w,k}/M_{w,k}$.

2.4. Droplet suspension strategy

From an experimental standpoint, droplets in normal gravity conditions are investigated by suspending them on a solid fiber. In this work, we propose a strategy to reproduce that configuration, combining the droplet suspension method with the evaporation model discussed in the previous sections. Physically, the droplet remains suspended on a solid fiber due to the interaction between the surface tension force of the liquid droplet and the surface of the solid fiber. In our model, the surface tension force in Eq. (20) is computed as $\mathbf{f}_\sigma = \sigma\kappa\nabla H$, where σ is the surface tension coefficient, which is constant, while the curvature κ is obtained from the height function. The combination of the resulting curvature and a well-balanced discretization of the gradients lead to the accurate numerical description of the surface tension [47]. The concept of height function is closely related to the height of the fluid interface. Therefore, knowing the height function is equivalent to knowing the position of the interface, and vice-versa. In a droplet suspension problem we know the coordinate $\mathbf{x}_p$ at which the interface must remain throughout the simulation. Physically, this *pinning point* corresponds to the gas–liquid–solid contact point. Therefore, we suspend the droplet by setting a Dirichlet boundary condition on the height-function h at the contact point, and a Neumann boundary condition elsewhere:

$$\begin{cases} h = \mathbf{x}_p & \text{if } \mathbf{x} = \mathbf{x}_p \\ \partial_n h = 0 & \text{elsewhere} \end{cases} \tag{29}$$

where ∂_n denotes the derivative along the normal direction of the boundary. The numerical implementation of the height functions on an adaptive computational grid was described by Popinet [47]. According to that formalism, the height function, in each interfacial cell, gives the distance of the closest interface from the center of the cell. Therefore, implementing the boundary conditions in Eq. (29) is achieved by
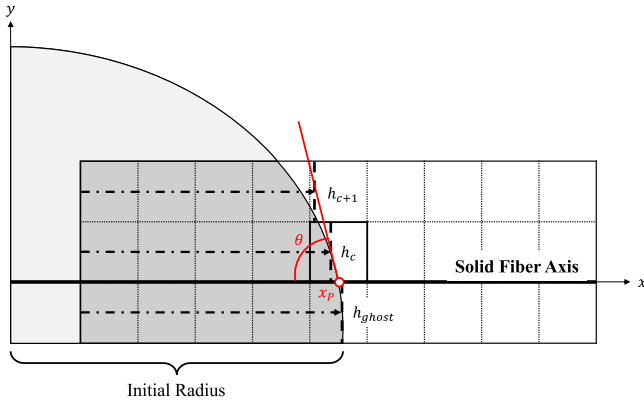
Fig. 2. Schematic representation of the height function boundary conditions, where the black line represents the solid fiber surface, the white point is the pinning point $\mathbf{x}_p$, while θ is the contact angle.

setting the value of the height function on the layer of ghost cells in contact with the droplet (Fig. 2):

$$(h_x)_{ghost} = \begin{cases} -(h_x)_c + 2(\mathbf{x}_p - \mathbf{x})/\Delta & \text{if } \mathbf{x} \geq \mathbf{x}_p \\ (h_x)_c & \text{elsewhere} \end{cases} \tag{30}$$

where the suffix c indicates a generic cell of the domain in contact with a ghost cell where we apply the boundary condition, while Δ is the cell dimension.

After setting this boundary condition, the curvature is computed as a function of the first and second derivatives of the height function:

$$\kappa = \frac{h''}{(1 + h'^2)^{3/2}} + \frac{1}{|\mathbf{x}| \sqrt{1 + h'^2}} \tag{31}$$

The resulting curvature is affected by the height function boundary condition, and the contact angle is dynamically adjusted according to the coordinate of the pinning point.

2.5. Numerical discretization details

The governing equations introduced in Section 2.2 are discretized on an adaptive Cartesian grid using the Finite Volume Method [48]. The characteristic function, in the context of the volume-of-fluid approach, is discretized using the volume fraction c, defined as:

$$c = \frac{1}{V} \int_V H \, dV = \frac{V_l}{V} \tag{32}$$

where V_l is the total volume of liquid in a computational cell, while V is the volume of the cell itself. Applying this definition to the interface transport Eq. (15), we obtain:

$$\frac{\partial c}{\partial t} + \frac{1}{V} \oint_S H \mathbf{u}_l \cdot \mathbf{n} \, dS = \frac{1}{V} \int_V H \nabla \cdot \mathbf{u}_l \, dV - \frac{1}{V} \int_V \frac{\dot{m}}{\rho_l} \delta_\Gamma \, dV \tag{33}$$

The purpose of the geometric volume-of-fluid is to directly discretize the integrals in this equation, maintaining the sharp nature of the characteristic function H by exploiting the explicit interface reconstruction [34]. For the sake of simplicity, in this section we substitute this equation with the notational form:

$$\frac{\partial c}{\partial t} + \nabla \cdot (c \mathbf{u}_l) = c \nabla \cdot \mathbf{u}_l - \frac{\dot{m}}{\rho_l} \delta_\Gamma \tag{34}$$

although the actual discretization does not use the volume fraction values directly in the divergence terms. The same logic applies to every other scalar transport equation, where the phase volume fraction c_k is introduced: $c_l = c$, $c_g = 1 - c$.

The governing Eqs. (15)–(20) are decoupled and solved in a sequential manner, using a time staggered scheme. Here, we briefly summarize the integration order, using the same formalism adopted by Popinet

[49], which assumes that the scalar fields (liquid volume fraction, temperature, and mass fractions) are known at the beginning of the time step at the time level $n - 1/2$, *i.e.* lagging behind the velocity and pressure fields by half time step. For brevity of notation, in the next steps, we do not indicate the time level for the phase properties in the transport equations. These properties are updated and known at time level $n - 1/2$.

1. At the beginning of the time step, the interface jump condition (Eq. (21)) is resolved using the same procedure explained by Cipriano et al. [24], in order to obtain the vaporization rates $\dot{m}_i^{n-1/2}$, the interface temperature $\hat{T}^{n-1/2}$, and the interface mass fractions $\hat{\omega}_{i,k}^{n-1/2}$. In each interfacial cell, the liquid mass fraction is assumed to be the interfacial mass fraction $\hat{\omega}_{i,l}$. The mass fraction is converted into mole fraction $\hat{x}_{i,l}$ and the thermodynamic equilibrium condition is used to calculate the gas phase interface mole fraction $\hat{x}_{i,g} = P_{vap,i}(\hat{T})/P\hat{x}_{i,l}$. The conversion to $\hat{\omega}_{i,g}$ is used for the calculation of the total vaporization rate:

$$\dot{m} = \frac{\sum_{i=1}^{NLS} \mathbf{j}_{i,g} \cdot \mathbf{n}_\Gamma}{1 - \sum_{i=1}^{NLS} \hat{\omega}_{i,g}} \tag{35}$$

   and the vaporization rate for each chemical species is updated as:

$$\dot{m}_i = \dot{m} \hat{\omega}_{i,g} + \mathbf{j}_{i,g} \cdot \mathbf{n}_\Gamma \tag{36}$$

   The interface temperature is computed from the vaporization rates by zeroing the non-linear equation given by the interface energy balance:

$$f(\hat{T}) = \sum_{i=1}^{NLS} \dot{m}_i \Delta h_{ev,i} + \dot{q}_{rad} - \lambda_l \nabla T_g \cdot \mathbf{n}_\Gamma + \lambda_g \nabla T_l \cdot \mathbf{n}_\Gamma = 0 \tag{37}$$

   Further details are explained in [24]. It is important to note that the calculation of the vaporization rate is obtained directly from interface gradients (computed as explained in [24,50]), and do not rely on sub-grid-scale correlations.

2. The phase properties are updated based on the thermodynamic pressure, and the current temperature and mass fraction fields:

$$\phi_k^{n-1/2} = f(P, T_k^{n-1/2}, \mathbf{x}_k^{n-1/2}) \tag{38}$$

3. The divergence source term is computed for each phase and the one-field divergence is obtained from the arithmetic average.

$$-\frac{1}{\rho} \frac{D\rho}{Dt} \bigg|_k^{n-1/2} = \frac{\beta_k}{\rho_k C p_k} \left[\nabla \cdot (c_k \lambda \nabla T_k) - \left(\sum_{i=1}^{NS} c_k C p_{i,k} \mathbf{j}_{i,k} \right) \cdot \nabla T_k + \dot{q}_{\Gamma,k} \delta_\Gamma \right]$$
$$+ \frac{M_{w,k}}{\rho_k} \sum_{i=1}^{NS} \frac{1}{M_{w,i}} \left[\nabla \cdot (c_k \mathbf{j}_{i,k}) + \dot{m} \omega_i \delta_\Gamma - \dot{m}_i \delta_\Gamma \right] \tag{39}$$

4. The advection of the volume fraction and of the scalar transport equations is solved, considering the generic scalar $s = \omega_i, T$:

$$\frac{c^{n+1/2} - c^{n-1/2}}{\Delta t} + \nabla \cdot (c \mathbf{u}_\Gamma)^n = c \nabla \cdot \mathbf{u}_\Gamma^n \tag{40}$$

$$\frac{(c_k s_k)^* - (c_k s_k)^{n-1/2}}{\Delta t} + \nabla \cdot (c_k s_k \mathbf{u}_k)^n = c_k s_k \nabla \cdot \mathbf{u}_k^n \tag{41}$$

5. The mass fractions are updated including the additional term stemming from the diffusion correction and the conversion from mole fraction gradients to mass fraction gradients:

$$\frac{(c_k \omega_{i,k})^{**} - (c_k \omega_{i,k})^*}{\Delta t} = \nabla \cdot \left[c_k \left(\mathbf{j}_{i,k}^M + \mathbf{j}_{i,k}^C \right) \omega_{i,k} \right]^* \tag{42}$$

6. The diffusion part of the chemical species and temperature equations is solved in an implicit manner, including the phase

change source terms:

$$c_k \rho_k \frac{\omega_{i,k}^{n+1/2} - \omega_{i,k}^{**}}{\Delta t} = \nabla \cdot \left(c_k \rho_k \mathcal{D}_{i,k} \nabla \omega_{i,k}^{n+1/2} \right) \tag{43}$$
$$+ (\dot{m} \delta_\Gamma)^{n-1/2} \omega_{i,k}^{n+1/2} - (\dot{m}_i \delta_\Gamma)^{n-1/2}$$

$$c_k \rho_k C p_k \frac{T_k^{n+1/2} - T_k^*}{\Delta t} = \nabla \cdot \left(c_k \lambda_k \nabla T_k^{n+1/2} \right)$$
$$- \left(\sum_{i=1}^{NS} c_k C p_{i,k} \mathbf{j}_{i,k} \right) \cdot \nabla T_k^{n-1/2} + (\dot{q}_{\Gamma,k} \delta_\Gamma)^{n-1/2}$$
$$\tag{44}$$

7. The droplet suspension is applied by enforcing the height function boundary conditions (Eq. (30)), and then the curvature κ is calculated (Eq. (31)).

8. The one-field properties ρ and μ are updated at the time level $n + 1/2$ from the respective phase properties using an arithmetic average, and the Navier–Stokes equations are solved for each phase:

$$\rho^{n+1/2} \left(\frac{\mathbf{u}_k^* - \mathbf{u}_k^n}{\Delta t} + (\mathbf{u}_k \cdot \nabla \mathbf{u}_k)^{n+1/2} \right) = -\nabla \cdot \tau_k^{n+1/2} \tag{45}$$

$$\rho^{n+1/2} \frac{\mathbf{u}_k^{**} - \mathbf{u}_k^*}{\Delta t} = \left(\sigma \kappa - \dot{m}^2 \left[1/\rho \right]_\Gamma \right) \nabla c^{n+1/2} - \mathbf{g} \cdot \mathbf{x} \nabla \rho^{n+1/2} \tag{46}$$

$$\nabla \cdot \left(\frac{1}{\rho^{n+1/2}} \nabla p_d^{n+1} \right) = \frac{\nabla \cdot \mathbf{u}^{**}}{\Delta t} + \frac{1}{\Delta t} \left(\frac{1}{\rho} \frac{D\rho}{Dt} \right)^{n-1/2} \tag{47}$$

$$\mathbf{u}_k^{n+1} = \mathbf{u}_k^{**} - \frac{\Delta t}{\rho^{n+1/2}} \nabla p_d^{n+1} \tag{48}$$

where the velocity jump (Eq. (7)) is imposed directly to the velocity fields $\mathbf{u}_l$ and $\mathbf{u}_g$ using the ghost velocity approach proposed by Tanguy et al. [15]. As advocated by Long et al. [51], this method can be conveniently combined with a collocated Navier–Stokes equations solver, limiting the oscillations in the velocity field that arise when including a localized divergence source term directly in the Poisson equation. This approach is based on the idea of Nguyen et al. [52] to use the Ghost Fluid Method to populate the velocity values on each side of the interface, obtaining two velocities $\mathbf{u}_l$ and $\mathbf{u}_g$ which are both continuous across the interface and which respect the correct jump condition (Eq. (7)):

$$\mathbf{u}_l = \begin{cases} \mathbf{u}_l & \text{if liquid phase} \\ \mathbf{u}_g + \dot{m} \left[1/\rho \right]_\Gamma \mathbf{n}_\Gamma & \text{if gas phase} \end{cases} \tag{49}$$

$$\mathbf{u}_g = \begin{cases} \mathbf{u}_g & \text{if gas phase} \\ \mathbf{u}_l - \dot{m} \left[1/\rho \right]_\Gamma \mathbf{n}_\Gamma & \text{if liquid phase} \end{cases} \tag{50}$$

with this condition enforced in the liquid and gas phase velocities after every solution step of Eqs. (45)–(48). Consequently, the divergence in Eq. (47) reads:

$$\nabla \cdot \mathbf{u}^{**} = \begin{cases} \nabla \cdot \mathbf{u}_l^{**} & \text{if liquid phase} \\ \nabla \cdot \mathbf{u}_g^{**} & \text{if gas phase} \end{cases} \tag{51}$$

The resulting liquid velocity, used for the transport of the volume fraction, is eventually corrected by additional projection steps in order to guarantee the correct divergence, as proposed by Tanguy et al. [15]. For constant properties simulations, the divergence of the liquid velocity is null, while for the variable properties formulation developed in this work, the divergence of the liquid velocity equals the Lagrangian derivative of the density in liquid phase. If the additional projections are neglected, the droplet evaporation problem cannot be solved accurately, conversely from the boiling problem [53]. Note that this method requires the vaporization rate $\dot{m}$, defined on the interfacial cells, to be extended toward the gas and the liquid phases. For this operation, we use PDE based extrapolation techniques [54], after converting the volume fraction field to a signed distance function [55].

3. Numerical results

The numerical model described in the previous section was implemented in the open-source code Basilisk [56]. The simulations performed using this model aim at the validation of the droplet suspension strategy (Section 3.1) and the low-Mach compressibility effects (Section 3.2). The simulation of n-heptane droplet evaporation in microgravity is presented in Section 3.3, comparing the model prediction with experimental data [3] and with the results from a well-validated spherically-symmetric model [12]. The effect of the introduction of gravity in the same test cases is presented in Section 3.4, focusing on the effect of the natural convective fluxes on the droplet consumption dynamics at different temperatures, pressures, and gravity values. The natural convective fluxes are also affected by the initial droplet diameter, as shown in Section 3.5, where our numerical model is compared with experiments of n-decane evaporation in normal gravity conditions [5]. The source code developed in this work, as well as the simulation setups are freely available on the Basilisk sandbox [57].

3.1. Equilibrium of a suspended droplet

This test case aims to validate the droplet suspension strategy. The starting point for the validation of every numerical method for surface tension is the analysis of a static isolated droplet, to verify that the numerical method is able to recover the equilibrium solution for a static droplet in microgravity (Laplace equation). Analogously, in this case we want to verify that the droplet, suspended at a specific point of the domain, can relax to the correct equilibrium position given by the balance between gravity and surface tension force. At the equilibrium conditions, the momentum Eq. (20) reduces to:

$$\nabla p_d = \left(\sigma \kappa - \dot{m}^2 [1/\rho]_\Gamma \right) \nabla c - \mathbf{g} \cdot \mathbf{x} \nabla \rho \tag{52}$$

Neglecting phase change, and considering a pure isothermal system, the one-field density ρ is a function of the volume fraction only. Therefore, Eq. (52) can be rewritten as:

$$\nabla p_d = \left(\sigma \kappa - [\rho]_\Gamma \mathbf{g} \cdot \mathbf{x} \right) \nabla c \tag{53}$$

which implies that, if the pressure and volume fraction gradients are discretized in the same way, the numerical scheme is well-balanced, and the equilibrium solution for the problem can be recovered [58].

The configuration used for this test case is depicted in Fig. 1(b), where half the droplet is initialized along a boundary of the domain. The initial droplet diameter is $D_0 = 1$ mm, and the physical properties are considered constant and equal to: $\rho_l = 1000$ kg m^{-3}, $\rho_g = 1$ kg m^{-3}, $\mu_l = 1 \times 10^{-3}$ Pa s, $\mu_g = 1 \times 10^{-5}$ Pa s. These properties are selected to mimic air–water properties, in order to test the suspension method using realistic density and viscosity ratios. The square domain has dimensions equal to $4D_0$, and the normal gravity value $\mathbf{g} = 9.81$ m s^{-2} is used. The droplet is initialized at coordinate $(0, 0)$, and the pinning point corresponds to the coordinate $(0.5D_0, 0)$ and it remains constant throughout the simulation. We use an adaptive grid with maximum level of refinement 8 (2^8 cells along each domain dimension). The simulation is performed in 2D and axial-symmetric (AXI) configurations, considering a fiber diameter for the AXI case equal to $D_f = 0.15D_0$. The simulation runs until the droplet reaches the equilibrium which, from the numerical point of view, was quantified by computing the total variation of volume fraction between two consecutive time steps. When this variation is smaller that the tolerance $\epsilon = 1 \times 10^{-10}$, the equilibrium configuration is reached and the simulation stops.

Fig. 3 reports the stationary shapes of the suspended droplet, for different values of surface tension σ. Increasing the surface tension, the droplet tends to a spherical shape, both in the planar (2D) and axial-symmetric (AXI) configuration. In the latter case, the droplet tends to always be more spherical due to the effect of the second curvature. Fig. 4(a) shows the quantitative comparison between the contact angle
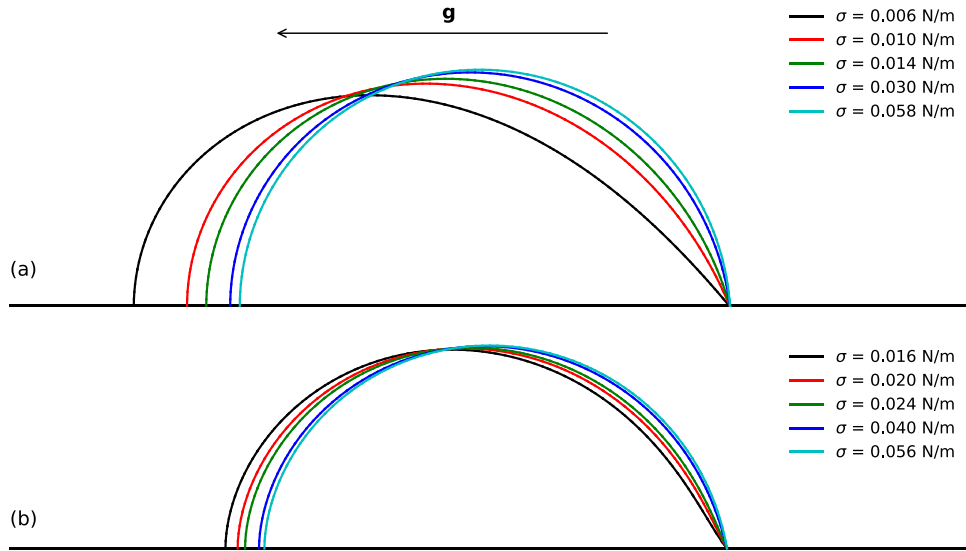
Fig. 3. Equilibrium shape for the 2D (a) and AXI (b) suspended droplets, with gravity pointing leftward with respect to the figures.
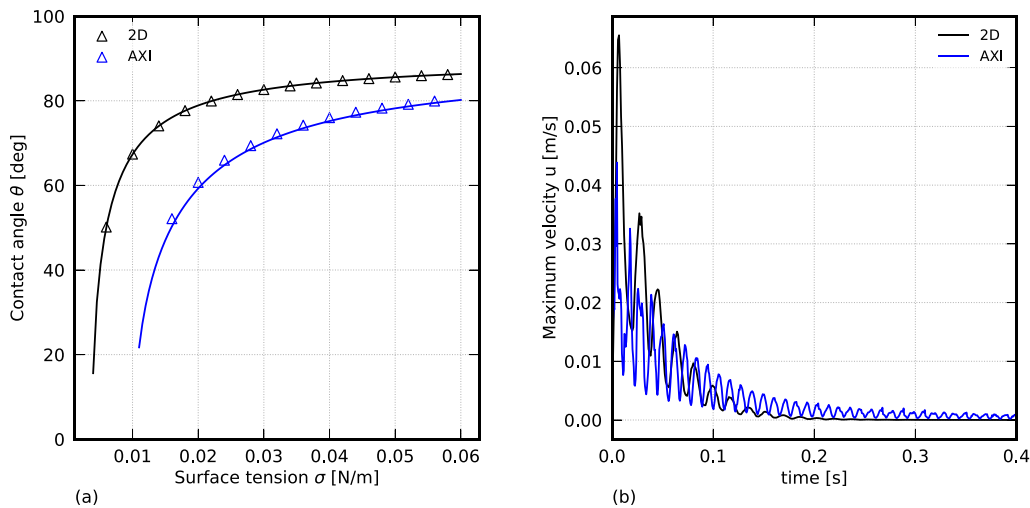

Fig. 4. Equilibrium contact angles, where the lines are the analytic solutions, while the markers are the numerical results (a); relaxation of the maximum velocity for the 2D and AXI cases (b) (http://basilisk.fr/sandbox/ecipriano/test/pinning.c).

of the stationary droplets from the numerical simulation and the analytical solution, calculated from the balance between surface tension force and gravity:

$$\theta_{2D} = \arccos\left(\frac{\rho_l g \pi (0.5 D_0)^2}{2\sigma}\right) \quad \theta_{AXI} = \arccos\left(\frac{4\rho_l g (0.5 D_0)^3}{3\sigma D_f}\right) \quad (54)$$

From Fig. 4(a) we can see that we obtain an excellent agreement between the numerical and analytical contact angles, both for the planar and AXI configurations, while Fig. 4(b) reports the relaxation of the maximum velocity toward null values for the cases with minimum surface tension coefficient, which are those that lead to stronger oscillations. The oscillatory behavior of the velocity field is due to the fact that, at the beginning of the simulation, the droplet tends to falls due to the effect of gravity and it is attracted back to the pinning point by the surface tension. The droplet keeps oscillating around the pinning position, until eventually reaching a steady position. Fig. 4(b) is a zoom of the oscillations region, where we observe that the AXI case takes more time to stabilize, but in both cases the velocity eventually tends toward a null value.

This test case confirms the ability of the suspension strategy to simulate droplets which relax toward an equilibrium position, respecting the analytical contact angle value.

3.2. Thermal expansion of a liquid droplet

In this test case we simulate the thermal expansion of an initially cold n-heptane droplet in a hot isothermal environment, neglecting the phase change. This test case is useful to assess the convergence of the model proposed in this work, with respect to the introduction of the density material derivative in Eq. (24), which is responsible for the droplet expansion. The droplet is initialized at the corner of a square domain, considering axial-symmetry and neglecting the gravitational term. The properties of this simulations are variable, therefore we do not initialize the material properties. Instead, we exploit the OpenSMOKE++ [37] library to initialize and update the properties according to the thermodynamic pressure, the temperature, and the mass fraction fields, as explained in Section 2.3. The droplet is considered to be pure n-heptane, while the gas phase is pure nitrogen. The initial droplet diameter is $D_0 = 1$ mm, while the domain length is equal to $1.5 D_0$. Symmetry boundary conditions are used for the
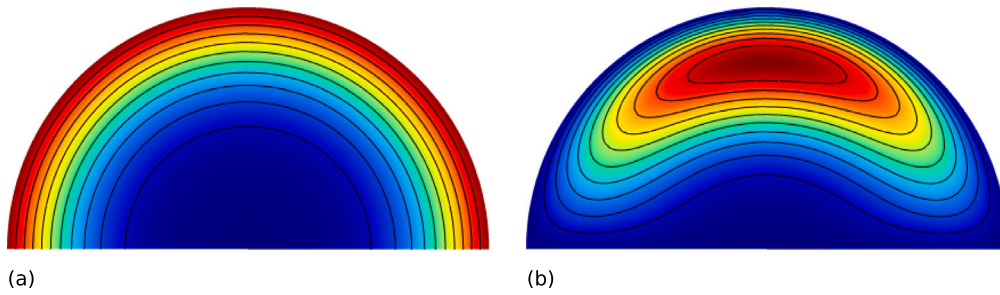
Fig. 5. Maps of the temperature (a) and velocity divergence (b) inside the liquid droplet, for the thermal expansion test case at time 0.1 s. The divergence field embeds the AXI metrics.
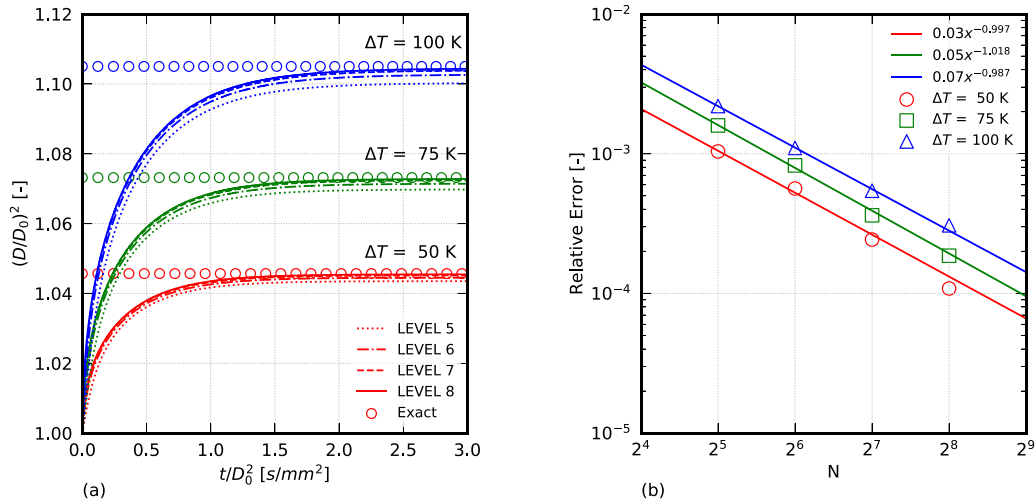

Fig. 6. Evolution of the normalized square diameter for the droplet expansion problem at different ΔT between the droplet and the environment (a); convergence rate for the droplet expansion problem (b) (http://basilisk.fr/sandbox/ecipriano/run/expansion.c).

two boundaries in contact with the droplet, while outflow boundary conditions for velocity and pressure are used for the other boundaries. The temperature of the liquid droplet is initialized at the value of 300 K, the thermodynamic pressure is considered constant and equal to 1.0 MPa. The simulation runs at three different ambient temperature: 350 K, 375 K, and 400 K, respectively. Each simulation runs for 3 s, a time which is sufficiently large to reach steady state conditions, and at four different levels of refinement (5, 6, 7, and 8).

At the beginning of the simulation, the droplet is heated by the isothermal environment, establishing a spherically-symmetric temperature profile inside the liquid droplet (Fig. 5(a)). The temperature gradients inside the liquid phase make the divergence source term (Eq. (24)) non-null (Fig. 5(b)), leading to the droplet expansion which compensates for density changes. In this simulation, not only the density changes, but also all the other properties involved. Therefore, the solution of the temperature field is performed using variable transport properties. Changing the properties affects the dynamic of the droplet expansion, but the droplet diameter at steady state D_s can easily be obtained by imposing that the mass of the liquid droplet must remain constant throughout the expansion process:

$$D_s = D_0 \left(\frac{\rho_l(T_l)}{\rho_l(T_g)} \right)^{1/3} \tag{55}$$

In this simulation, the density depends solely on temperature because the liquid is pure and the thermodynamic pressure is constant. Fig. 6(a) shows the trend of the droplet diameter in time obtained from the numerical simulation, and the steady state diameter for each initial ΔT between the droplet and the environment. We can see that, for each resolution, the temperature tends toward the steady-state value, as confirmed by Fig. 6(b), which reports the relative errors on the droplet

diameter at the four different levels of refinement. The error between the simulation and the stationary value increases with the initial temperature jump, but all three simulations converge with the same rate, which is extrapolated from the data and is approximately 1st order for each case under investigation. This test case confirms the convergence of the numerical schemes used to discretize the divergence source term, which allows the expansion of the droplet to be predicted correctly. This phenomenon is fundamental when studying the evaporation of liquid droplets in hot environments as shown in the next sections.

3.3. Evaporation of a n-heptane droplet in microgravity

Droplets in microgravity conditions have been studied in several experimental works, to isolate the evaporation phenomena from the influence of buoyancy-driven flows. This configuration is studied using drop towers, parabolic flights, or performing the experiment in orbiting spacecrafts [59]. In this section, we simulate the microgravity evaporation of isolated n-heptane droplets in nitrogen, and we compare the numerical results with experimental data by Nomura et al. [3], and with the 1D spherically-symmetric model by Cuoci et al. [12]. The experimental setup used by Nomura et al. [3] employs a drop tower and parabolic flights to achieve the reduced gravity conditions. The droplet is supported by an horizontal silica fiber with diameter of 150 μm, and experiments are performed at different ambient temperatures (from $\approx$ 450 K to $\approx$ 750 K), and at different pressure values ranging from 0.1 to 5 MPa. The droplet initial diameter is comprised between 0.6 and 0.8 mm. We simulate this configuration by placing the droplet at the corner of a square domain, considering a constant average initial diameter of 0.7 mm, and a domain length equal to 40 times the initial diameter, whose value is sufficiently large to avoid the influence of
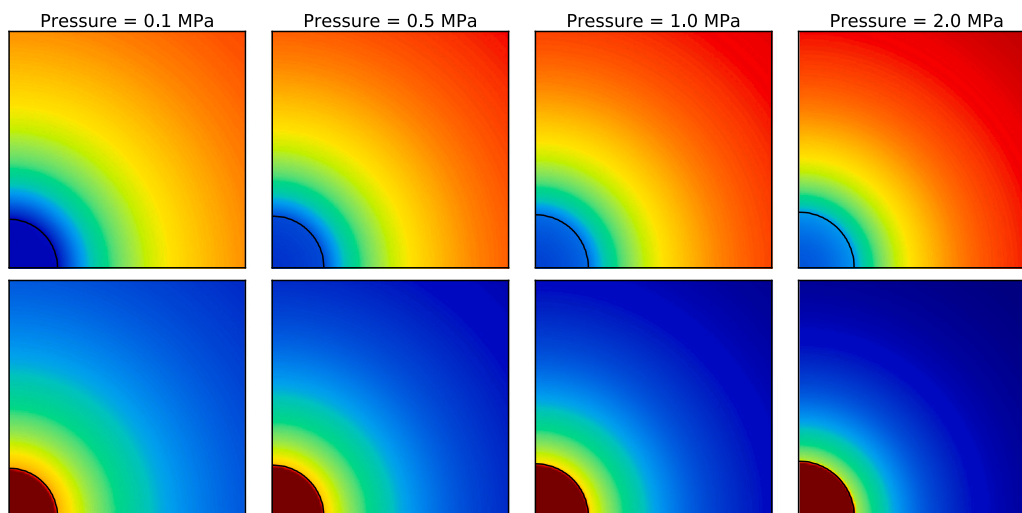
Fig. 7. Maps of temperature (top) and n-heptane mass fraction (bottom) at different ambient pressures in microgravity conditions at $T \approx 750$ K and time 0.6 s (http://basilisk.fr/sandbox/ecipriano/run/microgravity.c).

the boundaries on the dynamics of the droplet evaporation process. In these simulations, the use of an adaptive grid allows the large simulation domain to be maintained while limiting the computational burden. All the simulations presented in this section were performed at a maximum level of refinement equal to 11, using symmetry boundary conditions for the boundaries in contact with the liquid droplet, and outflow boundary conditions for the other sides of the domain. The experimental data provided by Nomura et al. [3] are known to be affected by radiation from the electric furnace walls to the surface of the droplet. This effect was studied by Yang and Wong [60], and it was included in these simulations according to Eq. (12), using an emissivity value for the n-heptane droplet which is constant and equal to $\epsilon = 0.93$, which is the same value used by Yang and Wong [60]. The surface tension coefficient is constant as well, and equal to $\sigma = 0.03$ N m^{-1}, while every other thermodynamic and transport property changes as described in Section 2.3. Initially, the environment is considered at rest, the liquid phase is made of pure n-heptane, while the gas phase is pure nitrogen. Among the experiments performed by Nomura et al. [3], we focus on the cases at 0.1 MPa, 0.5 MPa, 1 MPa, and 2 MPa, since experiments at 5 MPa are in supercritical conditions. For each pressure value we run 4 different simulations at 4 different ambient temperatures, ranging from ≈ 450 K to ≈ 750 K (the exact temperature values are reported in Fig. 8). Initially, the liquid phase temperature is equal to 300 K for every case under investigation.

The qualitative behavior of these simulations is similar for all the test cases: at the beginning of the simulation the hot environment heats the droplet, increasing the temperature of the liquid phase and causing thermal expansion. During this phase, the droplet diameter increases, leading to $(D/D_0)^2 > 1$, as shown in Fig. 8. As the interfacial temperature increases, the vaporization mass flow rate increases as well, until reaching a situation where the droplet consumption due to the evaporation process overtakes the droplet expansion with consequent decrease of the droplet diameter. After this transient, the squared diameter decay proceeds almost linearly, as predicted by the d^2 law, with a slope which is called *vaporization rate constant*. The intersection between the line that approximates the steady evaporation region, and the value $(D/D_0)^2 = 1$ defines a time coordinate called *heat-up period*, which measures the unsteadiness of the evaporation process [3]. From the knowledge of these two parameters, correlations that correct the classic d^2 law can be obtained, which are useful for sizing of engineering devices, or for simplified multiphase flow models.

Fig. 8 shows the comparison of the numerical model described in this work, with the experiments by Nomura et al. [3] and with the spherically-symmetric model by Cuoci et al. [12]. This model was

chosen because it was extensively validated under different operative conditions, in pure evaporation cases but also in combustion simulations [12,61,62]. The simulation results show that, for each pressure and temperature under investigation, the agreement between this work and the 1D model is always very good. These comparisons demonstrate the correct implementation of the variable properties extension to the multidimensional model proposed in this work. These results also highlight the role of temperature and pressure on the evaporation process in microgravity. For every ambient pressure, increasing the environment temperature increases the importance of the thermal expansion, which is observed from the higher peak of the square diameter. At the same time, higher temperatures reduce the heat-up period and increase the vaporization rate constant, leading to faster droplet consumption. The effect of the ambient pressure on the droplet consumption rate is less predictable and it depends on the ambient temperature. At the lower temperature ($T \approx 450$ K), increasing the pressure leads to stronger thermal expansion and an increased heat-up period, after which the vaporization rate constant is comparable for every pressure value. The ambient pressure increases the boiling point of the liquid droplet, which is allowed to reach higher temperature, as shown in the maps of Fig. 7. In these conditions, the ratio between the heat-up period and the total evaporation time remains approximately constant with pressure. Therefore, at lower temperature, an increase of pressure increases the droplet consumption time. At higher temperature ($T \approx 750$ K in this case), we observe that the vaporization rate constant increases with pressure and the final droplet consumption times are almost independent from the ambient pressure value. In these conditions, the ratio between the heat-up period and the total evaporation time increases with pressure.

The Schmidt number in the bulk gas phase for all these simulations varies from 2.2 for $T \approx 450$ K and it decreases with temperature up to 2.0 for $T \approx 750$ K, while remaining almost constant with pressure. The Lewis number slightly decreases with temperature as well going from 3 to 2.9 and indicating the greater importance of thermal diffusion with respect to the mass diffusion in gas phase. The average Sherwood number at ambient pressure increases with temperature from 3.8 to 6.4, due to the increased vaporization rate. Higher pressures decrease the Sh number up to 2.8 for the lowest temperature, and up to 5.7 to the highest temperature. These dimensionless numbers are calculated from their definitions:

$$Sc = \frac{\mu_g}{\rho_g D_g} \tag{56}$$

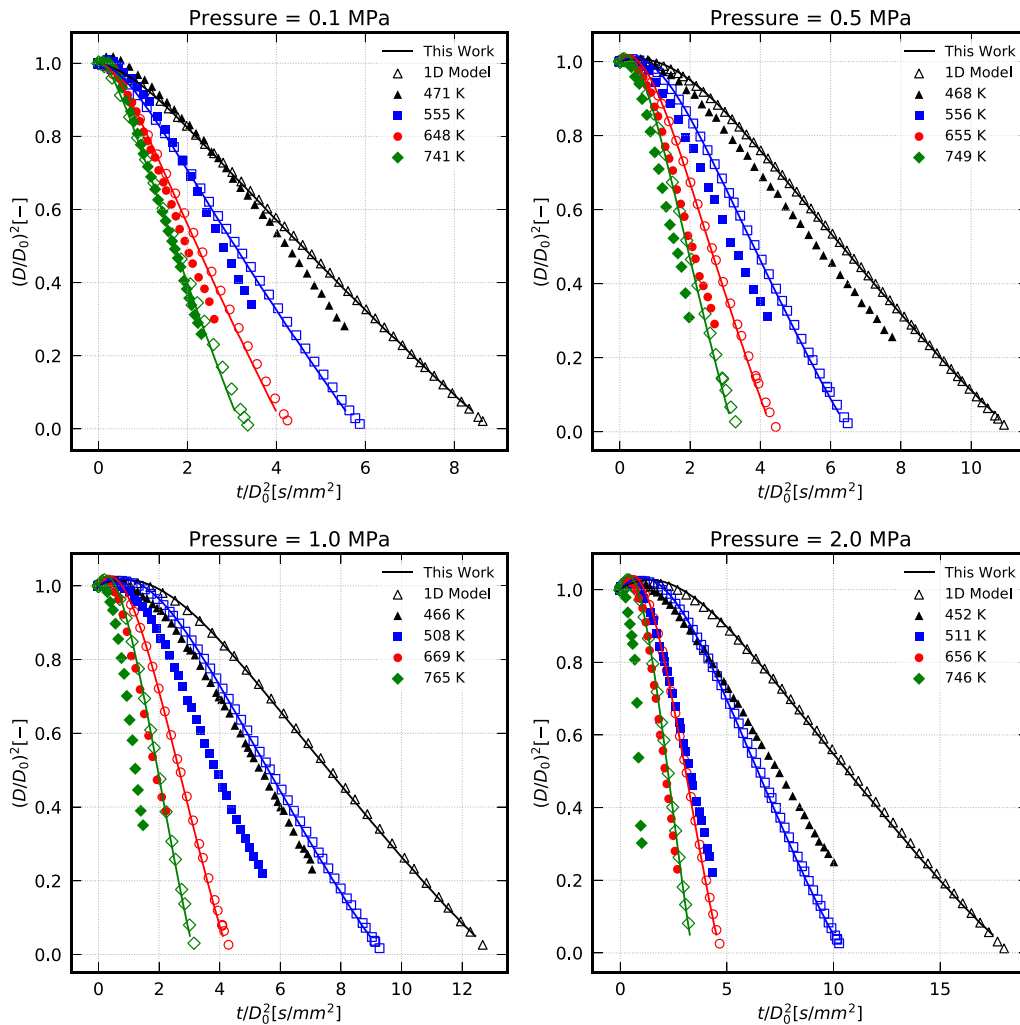$$Le = \frac{\lambda_g}{\rho_g D_g C p_g} \tag{57}$$

Fig. 8. Square diameter decay at different pressure and temperature for the microgravity evaporation of n-heptane. Comparison with experiments from Nomura et al. [3] (filled markers), and with the spherically-symmetric 1D model by Cuoci et al. [12] (empty markers) (http://basilisk.fr/sandbox/ecipriano/run/microgravity.c).

$$Sh = \frac{\dot{m}D}{(\hat{\omega}_{C_7,g} - \omega_{C_7,g})\rho_g D_g} \tag{58}$$

Although the comparison between this work and the 1D model shows good agreement, the comparison with the experimental data is not as good. At ambient pressure, the consumption curve of the numerical models is comparable with the experiments. Increasing the ambient pressure, the numerical models are systematically slower than the experiments, for every ambient temperature, and the displacement increases with pressure. Similar results were observed by other literature works [60,63,64]. In the next section, we propose possible explanations to this discrepancy, exploiting the capability of this numerical model to simulate the influence of buoyancy-driven flows on the droplet evaporation phenomena.

3.4. Effect of gravity on the evaporation of n-heptane droplets

The experimental data by Nomura et al. [3] were used by several authors for the validation of their droplet evaporation models. Some of them use just the low pressure results. Some other authors, such as Harstad and Bellan [63], Yang and Wong [60], and Gogos et al. [64], analyzed the trend of the droplet consumption at different pressure values. These authors obtained discrepancies between their models and the experimental data, which are similar to those shown in the previous section, and they propose possible explanations to these gaps based on the effect of the interface radiation, the heat conduction between

the gas–liquid system and the solid fiber [60], and the initial droplet positioning procedure [63,64]. Using the model proposed in this work, we can relax the hypothesis of spherical droplets and resolve the effect of buoyancy directly, demonstrating for the first time that the effect of residual gravity on the droplet evaporation results is non-negligible.

The simulations performed in this section combine the variable properties evaporation model with the droplet suspension strategy. Half the liquid droplet is initialized on the boundary of the domain corresponding to the axis of symmetry, and simulations exploit axial symmetry (valid for small Reynolds numbers) to limit the computational time. The simulation setup is depicted in Fig. 1(b), while the problem dimensions and the operative conditions are those used for the microgravity cases in Section 3.3. The only difference with respect to the microgravity cases is that we replicate those test cases using different gravity values: 1/100 **g**, 1/10 **g**, and 1 **g**, where **g** is the Earth's normal gravity. Note that the value of 1/100 **g** corresponds to the maximum values of residual gravity measured by Nomura et al. [3] for the parabolic flight experiments. The boundary of the domain in contact with the liquid droplet corresponds to the solid fiber surface, where no-slip boundary conditions are imposed, together with the height function boundary condition for the droplet suspension (Section 2.4). On the other sides of the domain we set zero pressure outflow boundary conditions for the velocity and the pressure fields.

At the beginning of the simulation, the droplet is heated by the hot environment, causing the thermal expansion of the droplet and increasing the vaporization rate. The phase change process cools down the
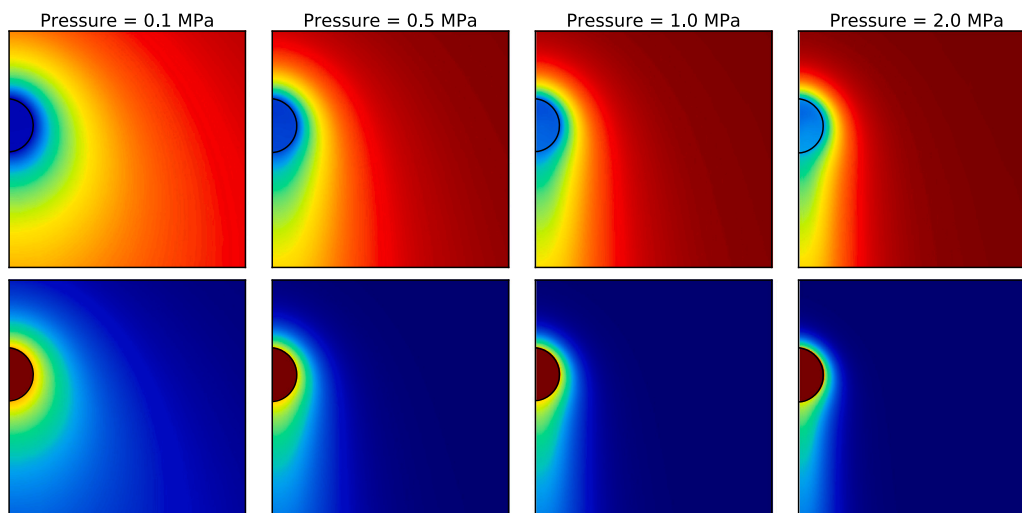
Fig. 9. Maps of temperature (top) and n-heptane mass fraction (bottom) at different ambient pressures in normal gravity conditions at time 0.6 s (http://basilisk.fr/sandbox/ecipriano/run/normalgravity.c).

interface and increases the amount of (cold) n-heptane in the gas phase, which is heavier than the hot nitrogen environment. Consequently, the gas phase density around the droplet increases with respect to the bulk gas density. The resulting density gradients promote buoyancy-driven flows, which create a downward wake that transports temperature and mass fraction fields as shown in Fig. 9. The importance of the buoyancy driven flows can be quantified using the Grashof number, defined as:

$$Gr = \frac{(\rho_s - \rho_b)}{\rho_b \nu_b^2} g D^3 \tag{59}$$

where ρ_s is the density of the gas phase at the interface, ρ_b is the bulk density, while the bulk kinematic viscosity is defined as $\nu = \mu/\rho$. The Grashof number is directly proportional to P^2, it increases with the gravity value and with the droplet diameter, and it decreases non-linearly with increasing ambient temperature. The mixture molecular weight of the gas phase increases the Grashof number as well, which becomes more important for heavier liquid droplets. Increasing the Grashof number, the acceleration of the fluid promoted by natural convective fluxes becomes larger. Fig. 9 clearly shows this effect: the image displays the maps of temperature and n-heptane mass fractions at the same simulation time (0.6 s) for different pressure values. Increasing the pressure, the Stefan flow contribution is lower, while the gas phase velocity transports the scalar fields downward more quickly, the boundary layer around the droplet becomes thinner, and these phenomena influence the droplet consumption dynamics. Fig. 10(a) shows the squared diameter decay for the Nomura et al. [3] droplets at different values of residual gravity. For improved readability we only included results at two temperature values for each pressure analyzed in the previous section. We observe that, in every simulation, the introduction of gravity increases the droplet consumption rate, with different magnitude depending on the operative conditions. At ambient pressure, gravity does not significantly affect the simulation results, especially for low residual gravity. However, at higher pressure the gap between the microgravity results increases quickly, and even a residual gravity of just $1/100$ **g** decreases the droplet lifetime considerably. We observe from the results in Fig. 10 that this effect is more important at high pressure and low ambient temperature, as predicted by the functional dependency of the Grashof number. Fig. 10(b) reports the normalized total evaporation time for every pressure and temperature analyzed in this study, and for the three gravitational values. The total evaporation time is extracted from the plots by reconstructing the line describing the squared diameter decay in the steady region. Therefore, the total evaporation time is computed as the intersection between the

reconstructed line and the coordinate corresponding to the complete droplet consumption $((D/D_0)^2 = 0)$. The normalized total evaporation time plotted in Fig. 10(b) is finally obtained as the ratio between the total evaporation time with gravity and the total evaporation time in microgravity, at the same conditions of temperature and pressure. By doing so, the resulting figure allows the displacement between the microgravity case and the gravity cases with increasing ambient temperature and pressure to be easily observed.

Including gravity, the Sc and Le numbers of the bulk gas phase are the same reported for the microgravity case at the previous section. However, the Sh number increases due to the effect of the natural convective fluxes. At ambient pressure in normal gravity Sh is equal to 5.4 at low temperature and to 8.8 at high temperature. Conversely from the microgravity case, its value increases with increasing ambient pressure for all temperatures investigated. Considering the 2 MPa case, it goes from 5.8 at low temperature to 9.3 at high temperature.

From the results in this section we can draw interesting conclusions that complete the analysis began by Yang and Wong [60]. In that work, the authors show that including radiation and the thermal effect from the solid fiber reduces the gap between the numerical results and the experiments. They show that the solid fiber effect is more important at low temperature, while the effect of the radiation is dominant for the high temperature simulations. The two effects tend to increase the droplet consumption rate in every simulation, and while they approximate the experimental data well at ambient pressure and sufficiently well at 0.5 MPa, they are not sufficient to explain the discrepancies at higher pressures. This work clearly shows that the discrepancy at higher pressure is due to the effect of the residual gravity, which is non-negligible for high pressures especially at the lower temperatures. It is worth mentioning that the axial-symmetric model proposed by Gogos et al. [64] was used by the authors to re-simulate the experiments by Nomura et al. [3] using normal gravity conditions, and obtaining a droplet consumption rate which is faster than the microgravity case and closer to the experimental data. The difference with that work is that here we tested the effect of small residual gravity values, and that our model directly resolves the interface deformation and is more generally applicable to any gas–liquid system with phase change. Moreover, Gogos et al. [64] indicated the procedure used to move the droplet from the droplet generator to the testing position as a possible additional explanation to the delay of the numerical results. The authors quantified this process stating that it induced droplet motion with an average velocity of 0.375 m/s for 0.16 s. To try to mimic the effect of this process, we initialized the
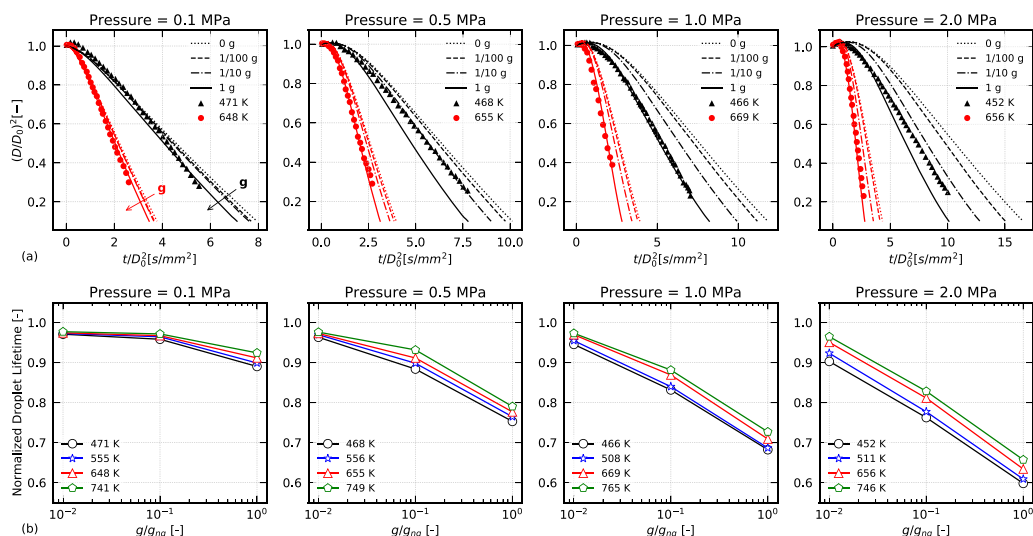
Fig. 10. Squared diameter decay at different pressure and temperature, and at 4 different gravitational acceleration values. The triangles are experiments from Nomura et al. [3] (a); Normalized total evaporation times (b) (http://basilisk.fr/sandbox/ecipriano/run/normalgravity.c).

velocity field of the droplet using a Hill's vortex considering a bulk velocity of 0.375 m/s. However, this procedure did not change the droplet dynamics, compared with the cases where the initial velocity is null everywhere (which is the initial setup for the results presented in this section).

An additional reason for the discrepancy between the numerical results and the experiments might be the use of an average initial diameter, which is equal for every simulation, since Nomura et al. [3] did not provide a specific initial diameter value for every simulation. However, when buoyancy is present, the initial diameter is an additional parameter that changes the importance of natural convective fluxes. This effect is studied in the next section.

3.5. Effect of the initial diameter on the evaporation of n-decane droplets

In the previous section, we studied the effect of the Grashof number on the evaporation of n-heptane droplets. We analyzed the influence of the ambient temperature, pressure, and the gravitational acceleration on the square diameter decay, and we compared the results with experiments of droplets in reduced gravity conditions. In this section, we study the effect of the initial diameter on the consumption of n-decane droplets in normal gravity conditions. This configuration was studied with experiments by Murakami et al. [5], providing the experimental data that we use here to verify the validity of our model's predictions.

The simulation setup is the same used in the previous section, and it is depicted in Fig. 1(b): it consists in initializing half the liquid droplet along the boundary corresponding to the axis of symmetry. The initial ambient and droplet temperatures are equal to 773 K, and 328 K, respectively. The droplet is pure n-decane, while the environment is initially pure nitrogen. No-slip boundary conditions are imposed on the boundary in contact with the liquid droplet, while constant pressure outflow boundary conditions are used for the other boundaries. The initial diameter of the droplet varies in the range between 0.4 and 0.8 mm, and simulations are performed at 4 different values of initial diameter, each at ambient pressure and at 0.5 MPa.

The numerical simulation results are compared with the experimental data in normal gravity conditions by Murakami et al. [5], and the comparison is shown in Fig. 11(a). The results indicate that an increase in the droplet's initial diameter enhances the significance of buoyancy-driven flows, making the vaporization rate constant steeper. This effect can be easily predicted by looking at the Grashof number (Eq. (59)). Increasing the pressure (Fig. 11 (b)), the effect of the initial diameter

on the vaporization rate is magnified. The numerical results obtained using this model are in good agreement with the experimental data at atmospheric pressure, while at 0.5 MPa the numerical results display an increased heat-up period. In both cases, the distances between the curves at $D_0 = 0.4$ mm and $D_0 = 0.8$ mm in normal gravity are similar to the experimental data. The temperature profiles are reported just for the case with $D_0 = 0.52$ mm, but they are similar for every simulation since the initial droplet diameter, in these conditions, does not influence the droplet temperature substantially. The trends of the droplet temperature profiles shows that, as expected, the high pressure droplets reach higher temperatures, due to the increased boiling point. We capture the increased gap in the consumption rates for the higher pressure simulations, and the bigger distance between case $D_0 = 0.4$ mm in microgravity and the same case but in normal gravity, which shows that the introduction of gravity has a stronger effect on the vaporization rate constant, in these conditions, with respect to the increased initial diameter. Understanding the larger gap between experimental data and model at 0.5 MPa would require insights from other authors' simulation results. The discrepancy might be due to neglecting the thermal effects of the solid fiber or to the increased complexity of conducting experiments at higher pressure. In any case, the model predicts the correct trends at different pressure values.

For these simulations, the bulk Sc and Le numbers are equal to 2.5 and 3.5, respectively. In microgravity conditions, the average Sh number is 8.1 at 0.1 MPa and 7.3 at 0.5 MPa. When gravity is included, the Sh number at ambient pressure ranges from 8.4 to 8.9 as the initial diameter increases. At higher pressure, the Sh number increases with the initial diameter, ranging from 8.3 to 9.6.

This test case emphasizes the ability of the numerical model to predict the consumption rate of liquid droplets suspended in normal gravity conditions with good accuracy, capturing the correct experimental trends.

4. Concluding remarks

This work proposes and validates a numerical model that significantly advances our understanding of the evaporation dynamics of suspended droplets in various gravitational conditions.

1. The model integrates interface-resolved evaporation, surface tension effects, and variable physical properties. This comprehensive approach allows for the accurate simulation of complex phenomena such as thermal expansion, natural convective fluxes,
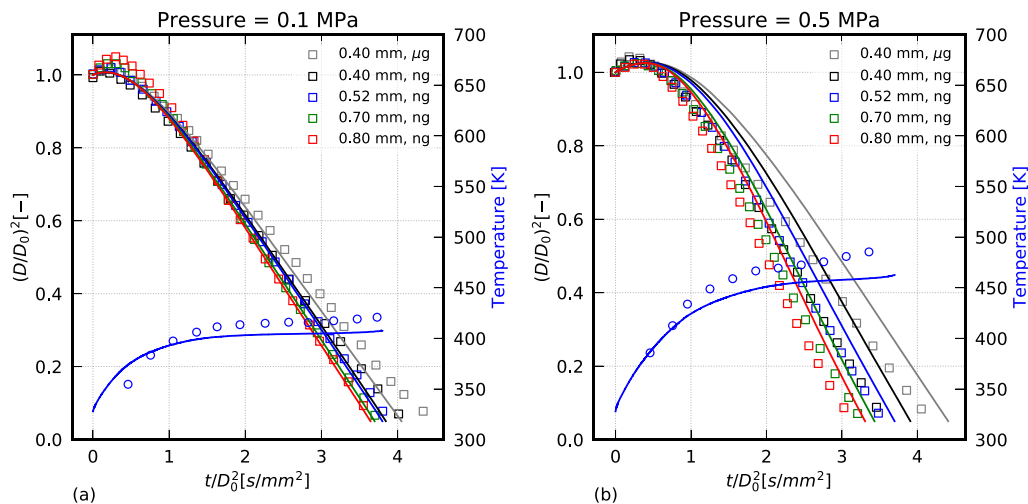
Fig. 11. Normalized squared diameter and temperature profile for the n-decane evaporation in normal gravity conditions (ng) and in microgravity (μg). Comparison with experiments by Murakami et al. [5] (http://basilisk.fr/sandbox/ecipriano/run/normalgravity.c).

and internal liquid recirculation, which are not addressed by traditional spherically-symmetric models.

2. The model's capability to simulate realistic droplet evaporation in any gravity condition has been demonstrated. For simulations involving gravity, a droplet suspension model was proposed that leverages surface tension without introducing fictitious forces. This model was validated by comparing the equilibrium contact angle with the analytical solution. Additionally, the variable properties evaporation model was benchmarked against experimental data in both microgravity and normal gravity conditions, as well as against a simplified spherically-symmetric model, showing very good agreement and validating the implementation of this work.

3. Comparisons with experimental data reveal discrepancies increasing with ambient pressure, consistently with findings from other studies in the literature. This study elucidates that such discrepancies can largely be attributed to the effects of residual gravity, in addition to thermal conduction from the solid fiber and interface radiation, as discussed by other researchers. The model also successfully compared with experimental data for suspended droplets in normal gravity conditions, enhancing predictive capabilities crucial for designing systems in aerospace and industrial manufacturing.

4. Future research will focus on extending the model to more complex fluids and environmental conditions, aiming to broaden its applicability and refine our ability to predict droplet behavior across a range of operational scenarios.

CRediT authorship contribution statement

Edoardo Cipriano: Writing – original draft, Visualization, Validation, Software, Methodology, Investigation, Formal analysis, Conceptualization. **Alessio Frassoldati:** Writing – review & editing, Supervision. **Tiziano Faravelli:** Writing – review & editing, Supervision. **Stéphane Popinet:** Writing – review & editing, Supervision. **Alberto Cuoci:** Writing – review & editing, Supervision, Conceptualization.

Declaration of competing interest

The authors declare the following financial interests/personal relationships which may be considered as potential competing interests: Edoardo Cipriano reports financial support was provided by European Union. If there are other authors, they declare that they have no known competing financial interests or personal relationships that could have appeared to influence the work reported in this paper.

Data availability

All the codes developed in this work and the simulation setup are released on the Basilisk website. The manuscript reports the relative links.

Acknowledgements

References

[1] E.L. Andreas, J.B. Edson, E.C. Monahan, M.P. Rouault, S.D. Smith, The spray contribution to net evaporation from the sea: A review of recent progress, Bound.-Layer Meteorol. 72 (1995) 3–52.

[2] W.A. Sirignano, Fluid Dynamics and Transport of Droplets and Sprays, Cambridge University Press, 2010.

[3] H. Nomura, Y. Ujiie, H.J. Rath, J. Sato, M. Kono, Experimental study on high-pressure droplet evaporation using microgravity conditions, in: Symposium (International) on Combustion, Vol. 26, No. 1, Elsevier, 1996, pp. 1267–1273.

[4] C. Verwey, M. Birouk, Experimental investigation of the effect of natural convection on the evaporation characteristics of small fuel droplets at moderately elevated temperature and pressure, Int. J. Heat Mass Transfer 118 (2018) 1046–1055.

[5] Y. Murakami, H. Nomura, Y. Suganuma, Experimental study on unsteadiness of n-decane single droplet evaporation and effect of natural convection on droplet evaporation and temperatures at high pressures and temperatures, Trans. Japan Soc. Aeronaut. Space Sci., Aerosp. Technol. Japan 19 (5) (2021) 647–653.

[6] H. Ghassemi, S.W. Baek, Q.S. Khan, Experimental study on binary droplet evaporation at elevated pressures and temperatures, Combust. Sci. Technol. 178 (6) (2006) 1031–1053.

[7] A. Daïf, M. Bouaziz, X. Chesneau, A.A. Cherif, Comparison of multicomponent fuel droplet vaporization experiments in forced convection with the sirignano model, Exp. Therm Fluid Sci. 18 (4) (1998) 282–290.

[8] D.L. Dietrich, V. Nayagam, M.C. Hicks, P.V. Ferkul, F.L. Dryer, T. Farouk, B.D. Shaw, H.K. Suh, M.Y. Choi, Y.C. Liu, et al., Droplet combustion experiments aboard the international space station, Microgravity Sci. Technol. 26 (2014) 65–76.

[9] Y. Liu, Y. Xu, C. Avedisian, M. Hicks, The effect of support fibers on micro-convection in droplet combustion experiments, Proc. Combust. Inst. 35 (2) (2015) 1709–1716.

[10] Y.C. Liu, Y. Xu, M.C. Hicks, C.T. Avedisian, Comprehensive study of initial diameter effects and other observations on convection-free droplet combustion in the standard atmosphere for n-heptane, n-octane, and n-decane, Combust. Flame 171 (2016) 27–41.

[11] A.K. Yadav, A. Chowdhury, A. Srivastava, Interferometric investigation of methanol droplet combustion in varying oxygen environments under normal gravity, Int. J. Heat Mass Transfer 111 (2017) 871–883.

[12] A. Cuoci, M. Mehl, G. Buzzi-Ferraris, T. Faravelli, D. Manca, E. Ranzi, Autoignition and burning rates of fuel droplets under microgravity, Combust. Flame 143 (3) (2005) 211–226.

[13] A.J. Marchese, F.L. Dryer, The effect of liquid mass transport on the combustion and extinction of bicomponent droplets of methanol and water, Combust. Flame 105 (1–2) (1996) 104–122.

[14] M. Irfan, M. Muradoglu, A front tracking method for direct numerical simulation of evaporation process in a multiphase system, J. Comput. Phys. 337 (2017) 132–153.

[15] S. Tanguy, T. Ménard, A. Berlemont, A level set method for vaporizing two-phase flows, J. Comput. Phys. 221 (2) (2007) 837–853.

[16] N. Scapin, P. Costa, L. Brandt, A volume-of-fluid method for interface-resolved simulations of phase-changing two-fluid flows, J. Comput. Phys. 407 (2020) 109251.

[17] L. Malan, A.G. Malan, S. Zaleski, P. Rousseau, A geometric VOF method for interface resolved phase change and conservative thermal energy advection, J. Comput. Phys. 426 (2021) 109920.

[18] J. Palmore Jr., O. Desjardins, A volume of fluid framework for interface-resolved simulations of vaporizing liquid-gas flows, J. Comput. Phys. 399 (2019) 108954.

[19] Y. Wang, X. Chen, X. Wang, V. Yang, Vaporization of liquid droplet with large deformation and high mass transfer rate, II: variable-density, variable-property case, J. Comput. Phys. 394 (2019) 1–17.

[20] N. Scapin, F. Dalla Barba, G. Lupo, M.E. Rosti, C. Duwig, L. Brandt, Finite-size evaporating droplets in weakly compressible homogeneous shear turbulence, J. Fluid Mech. 934 (2022) A15.

[21] G. Mialhe, S. Tanguy, L. Tranier, E.-R. Popescu, D. Legendre, An extended model for the direct numerical simulation of droplet evaporation. Influence of the Marangoni convection on leidenfrost droplet, J. Comput. Phys. 491 (2023) 112366.

[22] E.A. Wenzel, M. Arienti, A conservative, interface-resolved, compressible framework for the modeling and simulation of liquid/gas phase change, J. Comput. Phys. 477 (2023) 111957.

[23] M. Bibal, M. Deferrez, S. Tanguy, A. Urbano, A compressible solver for two phase-flows with phase change for bubble cavitation, J. Comput. Phys. 500 (2024) 112750.

[24] E. Cipriano, A.E. Saufi, A. Frassoldati, T. Faravelli, S. Popinet, A. Cuoci, Multicomponent droplet evaporation in a geometric volume-of-fluid framework, J. Comput. Phys. (ISSN: 0021-9991) 507 (2024) 112955.

[25] D.A. Drew, Mathematical modeling of two-phase flow, Annu. Rev. Fluid Mech. 15 (1) (1983) 261–291.

[26] R.B. Bird, Transport phenomena, Appl. Mech. Rev. 55 (1) (2002) R1–R4.

[27] T. Poinsot, D. Veynante, Theoretical and Numerical Combustion, RT Edwards, Inc., 2005.

[28] M. Ishii, T. Hibiki, Thermo-Fluid Dynamics of Two-Phase Flow, Springer Science & Business Media, 2010.

[29] V. Boniou, T. Schmitt, A. Vié, Consistency and accuracy in the simulation of two-phase flows with phase change using sharp interface capturing methods, J. Comput. Phys. 470 (2022) 111604.

[30] L. Thijs, C. Van Gool, W. Ramaekers, J.A. van Oijen, L. De Goey, Resolved simulations of single iron particle combustion and the release of nano-particles, Proc. Combust. Inst. 39 (3) (2023) 3551–3559.

[31] R.C. Reid, J.M. Prausnitz, B.E. Poling, The Properties of Gases and Liquids, McGraw Hill Book Co., New York, NY, 1987.

[32] R.P. Fedkiw, T. Aslam, B. Merriman, S. Osher, A non-oscillatory Eulerian approach to interfaces in multimaterial flows (the ghost fluid method), J. Comput. Phys. 152 (2) (1999) 457–492.

[33] R. Scardovelli, S. Zaleski, Direct numerical simulation of free-surface and interfacial flow, Annu. Rev. Fluid Mech. 31 (1) (1999) 567–603.

[34] V. Boniou, On the Numerical Simulation of Evaporating Two-Phase Flows Using Sharp Interface Capturing Methods (Ph.D. thesis), Université Paris-Saclay, 2021.

[35] G.H. Yeoh, J. Tu, Computational Techniques for Multiphase Flows, Butterworth-Heinemann, 2019.

[36] G. Tryggvason, R. Scardovelli, S. Zaleski, Direct Numerical Simulations of Gas–Liquid Multiphase Flows, Cambridge University Press, 2011.

[37] A. Cuoci, A. Frassoldati, T. Faravelli, E. Ranzi, OpenSMOKE++: An object-oriented framework for the numerical modeling of reactive systems with detailed kinetic mechanisms, Comput. Phys. Comm. 192 (2015) 237–264.

[38] R. Kee, F. Rupley, J. Miller, CHEMKIN: The chemkin thermodynamic database, 1987, Rep. SAND87-8215, Sandia National Laboratories, Livermore (CA), USA.

[39] H. Wang, M. Frenklach, Transport properties of polycyclic aromatic hydrocarbons for flame modeling, Combust. Flame 96 (1–2) (1994) 163–170.

[40] S. Benson, Thermochemical Kinetics, second ed., Wiley, New York, 1976.

[41] A. Cuoci, A. Frassoldati, T. Faravelli, E. Ranzi, A computational tool for the detailed kinetic modeling of laminar flames: Application to C2h4/CH4 coflow flames, Combust. Flame 160 (5) (2013) 870–886.

[42] R.B. Pember, L.H. Howell, J.B. Bell, P. Colella, W.Y. Crutchfield, W. Fiveland, J. Jessee, An adaptive projection method for unsteady, low-mach number combustion, Combust. Sci. Technol. 140 (1–6) (1998) 123–168.

[43] J. Bell, AMR for low mach number reacting flow, in: Adaptive Mesh Refinement-Theory and Applications: Proceedings of the Chicago Workshop on Adaptive Mesh Refinement Methods, Sept. 3–5, 2003, Springer, 2005, pp. 203–221.

[44] Y. Saade, D. Lohse, D. Fuster, A multigrid solver for the coupled pressure-temperature equations in an all-mach solver with VoF, J. Comput. Phys. 476 (2023) 111865.

[45] J.O. Hirschfelder, C.F. Curtiss, R.B. Bird, The Molecular Theory of Gases and Liquids, John Wiley & Sons, 1964.

[46] T. Coffee, J. Heimerl, Transport algorithms for premixed, laminar steady-state flames, Combust. Flame 43 (1981) 273–289.

[47] S. Popinet, An accurate adaptive solver for surface-tension-driven interfacial flows, J. Comput. Phys. 228 (16) (2009) 5838–5866.

[48] J.H. Ferziger, M. Perić, R.L. Street, Computational Methods for Fluid Dynamics, springer, 2019.

[49] S. Popinet, Gerris: a tree-based adaptive solver for the incompressible Euler equations in complex geometries, J. Comput. Phys. 190 (2) (2003) 572–600.

[50] S. Fleckenstein, D. Bothe, A volume-of-fluid-based numerical method for multi-component mass transfer with local volume changes, J. Comput. Phys. 301 (2015) 35–58.

[51] T. Long, J. Pan, S. Zaleski, An edge-based interface tracking (EBIT) method for multiphase flows with phase change, J. Comput. Phys. (ISSN: 0021-9991) 513 (2024) 113159.

[52] D.Q. Nguyen, R.P. Fedkiw, M. Kang, A boundary condition capturing method for incompressible flame discontinuities, J. Comput. Phys. 172 (1) (2001) 71–98.

[53] S. Tanguy, M. Sagan, B. Lalanne, F. Couderc, C. Colin, Benchmarks and numerical methods for the simulation of boiling flows, J. Comput. Phys. 264 (2014) 1–22.

[54] T.D. Aslam, A partial differential equation approach to multidimensional extrapolation, J. Comput. Phys. 193 (1) (2004) 349–355.

[55] A. Limare, S. Popinet, C. Josserand, Z. Xue, A. Ghigo, A hybrid level-set/embedded boundary method applied to solidification-melt problems, J. Comput. Phys. 474 (2023) 111829.

[56] S. Popinet, A quadtree-adaptive multigrid solver for the Serre–Green–Naghdi equations, J. Comput. Phys. 302 (2015) 336–358.

[57] E. Cipriano, Code repository, 2023, http://basilisk.fr/sandbox/ecipriano/.

[58] S. Popinet, Numerical models of surface tension, Annu. Rev. Fluid Mech. 50 (2018) 49–75.

[59] M.Y. Choi, F.L. Dryer, Microgravity droplet combustion, in: Microgravity Combustion: Fire in Free Fall, Combustion Treatise, Academic Press Cambridge, MA, USA, 2001, pp. 183–297.

[60] J.-R. Yang, S.-C. Wong, On the discrepancies between theoretical and experimental results for microgravity droplet evaporation, Int. J. Heat Mass Transfer 44 (23) (2001) 4433–4443.

[61] A. Cuoci, A. Frassoldati, T. Faravelli, E. Ranzi, Numerical modeling of autoignition of isolated fuel droplets in microgravity, Proc. Combust. Inst. 35 (2) (2015) 1621–1627.

[62] A. Nobili, A. Frassoldati, T. Faravelli, A. Cuoci, Soot formation in combustion of spherically symmetric isolated fuel droplets with different initial diameters, Fuel 363 (2024) 130403.

[63] K. Harstad, J. Bellan, An all-pressure fluid drop model applied to a binary mixture: heptane in nitrogen, Int. J. Multiph. Flow 26 (10) (2000) 1675–1706.

[64] G. Gogos, S. Soh, D.N. Pope, Effects of gravity and ambient pressure on liquid fuel droplet evaporation, Int. J. Heat Mass Transfer 46 (2) (2003) 283–296.